Laser optical pumping of high-density Rb in polarized ^{3}He targets

M. E. Wagshul*
Harvard University, Physics Department, Cambridge, Massachusetts 02138

T. E. Chupp
University of Michigan, Ann Arbor, Michigan 48109
(Received 18 October 1993)

We have investigated high-density Rb optical pumping in polarized ^{3}He targets and present measurements of collisional relaxation rates and studies of diffusion-driven wall relaxation of the Rb polarization. We show that a boundary layer resides in the vicinity of the cell walls within which a polarization gradient is established by diffusion. Absorption of the incident laser radiation within this layer leads to a striking decrease in optical-pumping efficiency for resonant light but has little effect for off-resonant light. Our theory introduces polarization-dependent slowing of optical pumping rates due to the Rb nuclear spin. We have observed a strong frequency dependence of the optical-pumping efficiency, consistent with our theoretical predictions. We report the following rate constants for collisional relaxation of Rb polarization: due to Rb ($k_{\text{Rb-Rb}}=8\times10^{-13}$ cm^3/s), due to N_2 ($k_{N_2\text{-Rb}}=8\times10^{-18}$ cm^3/s), and due to ^{3}He, an upper limit of ($k_{^3\text{He-Rb}}\leq2\times10^{-18}$ cm^3/s). The data and model presented are used to predict laser power and intensity requirements for high-density polarized ^{3}He targets.

PACS number(s): 32.80.Bx, 32.70.Jz

I. INTRODUCTION

The development of high-density (ten atmospheres and greater) polarized ^{3}He targets has made practical a host of new experiments which require volumes up to 100 cm^3, and ^{3}He polarizations of 50% or more. Polarized ^{3}He is an ideal tool for precision magnetometry applied to studies of the fundamental symmetries [1]. It is also possible to operate a steady-state ^{3}He Zeeman maser by coupling the ^{3}He magnetization to a resonant circuit; this also has application to improved precision magnetometry techniques [2–4]. Polarized ^{3}He targets have recently been developed for proton and pion scattering experiments [5], muon capture [6], and high-energy electron scattering [7–9].

The most successful approach for producing sufficiently high-density, highly polarized ^{3}He samples is spin exchange with optically pumped Rb vapor [10], first observed by Bouchiat, Carver, and Varnum [11]. Spin exchange between Rb and ^{3}He is mediated by the hyperfine interaction between the Rb valence electron and the ^{3}He nucleus, which is effective only for the duration of a binary collision. (For heavier noble gases, notably Xe and Rb-Xe, van der Waals molecules form which can greatly increase the duration of the effective hyperfine interaction [12,13].)

The rate constant for spin exchange is 1.2×10^{-19} cm^3/s, and therefore a dense Rb vapor ($[\text{Rb}]>4\times10^{14}$/cm^3) is required to produce spin-exchange times on the order of a few hours, which are necessary to produce high ^{3}He polarization [14]. (The longitudinal relaxation time for ^{3}He is limited by ^{3}He-^{3}He collisions to about 700 h/amagat [6,15], but is typically several tens of hours due to collisions with contaminants, wall relaxation, and magnetic-field gradients.) At this high Rb density, the large number of Rb atoms requires about 100–200 mW of laser power per cm^3, and the utilization of titanium-sapphire lasers has led to volumes and Rb densities sufficiently large for practical targets [6,7,16]. At these high Rb densities, limitations persist due to bulk and wall relaxation of spin-polarized Rb, and effects related to radiation trapping. As reported in previous papers, radiation trapping effects have been mitigated with a N_2 buffer gas that nonradiatively quenches the excited states of Rb [10]. Bulk relaxation, which follows from the spin-spin interaction between Rb atoms and from the much weaker spin-rotation interaction during Rb-buffer gas collisions, determines the total laser power needed.

The limitation to Rb optical pumping imposed by spin-relaxing cell walls manifests itself in a small boundary layer within which a polarization gradient is established by diffusion. In this layer, the dense alkali-metal vapor strongly absorbs the incident, polarized laser light and leads to the strong frequency dependence of optical-pumping efficiency illustrated in Fig. 1. In this figure we show the ^{3}He polarization rate which is proportional to the average Rb polarization in the cell. The striking resonant dip was first observed several years ago [17], and it has been practical to tune the incident light slightly off-resonance for increased Rb and ^{3}He polarization in polarized targets. We attribute this dip to the polarization gradient within the boundary layer. Also evident in Fig. 1 is the dependence of the ^{3}He polarization rate on Rb density.

To understand quantitatively this boundary layer and the fundamental limitations of the spin-exchange technique, we must quantify all elements of the spin-

*Present address: NIST, Gaithersburg, MD 20899.

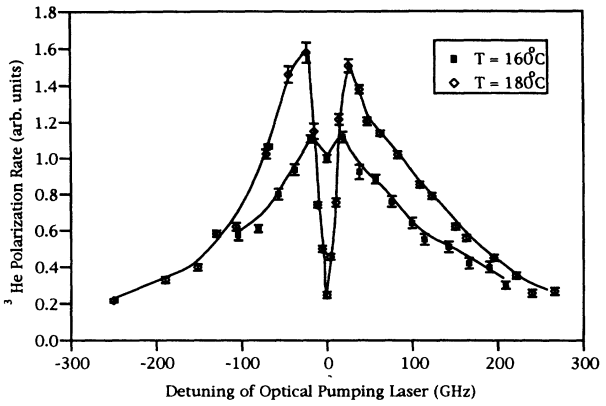

FIG. 1. Frequency and Rb density dependence of the optical-pumping efficiency evident in the ^{3}He polarization rate. The Rb densities are estimated to be 1×10^{14} and 4×10^{14}/cm^3, respectively, at 160°C and 180°C. This illustrates the importance of the resonant dip structure attributed to wall-induced relaxation and the bulk relaxation mechanisms.

exchange–optical-pumping process. The polarization of an optically dense alkali-metal vapor has not been treated adequately either experimentally or theoretically. In the limit of an optically thick vapor, the optical pumping-rate equations become nonlinear, and interpretation of data is often confusing, with the result that the optically dense regime of optical pumping has been avoided in the past. In this paper we review the theory of Rb optical pumping, introduce a polarization-dependent slowing factor into the rate equations, describe measurements of collisional relaxation rate constants, describe the theory of diffusion-driven wall relaxation, and present measurements that are in excellent agreement with modeling based on our theoretical framework and the measured bulk spin-relaxation rates. Finally, we show that these effects can have practical importance in the application of high-density optical pumping to the production of an efficient polarized ^{3}He target.

II. THEORY OF RB OPTICAL PUMPING OF RB

We consider optical pumping of Rb atoms on the $D1$ ($5s_{1/2}$-$5p_{1/2}$) transition in the presence of ^{3}He and N_2 buffer gases. A buffer gas of N_2 of 30–100 torr is typically added to the cells in order to nonradiatively quench the excited state; this minimizes the effects of radiation trapping. N_2 is used because it has a large quenching cross section: for N_2 pressures above 0.5 torr, this quenching rate exceeds the radiative decay rate.

The atoms are illuminated with circularly polarized σ_+ light, inducing only transitions satisfying the condition $\Delta m_s=+1$. Excited-state atoms undergo spin-nonconserving buffer gas collisions, predominantly with ^{3}He [18], and decay to either ground-state spin projection with equal probability. For the $D1$ transition, the atoms are pumped out of the $m_s=-\frac{1}{2}$ state, and the population is built up in the $m_s=+\frac{1}{2}$ state. For the $D2$ transition, atoms are pumped out of both ground-state spin projections in the ratio 1:2, respectively, for the $m_s=-\frac{1}{2}$ and $+\frac{1}{2}$ states. As a result the $D1$ transition can produce a maximum of +100% spin polarization of the Rb ground state, in contrast to the $D2$ transition for which the maximum polarization is −50%. (We note that the light intensity is typically many orders of magnitude below saturation for the collisionally broadened p state, and therefore that the excited-state population is negligible.)

A. Optical-pumping-rate equations

Consider the populations of the two ground states, $\rho_{+1/2}$ and $\rho_{-1/2}$, normalized to satisfy the condition $\rho_{+1/2}+\rho_{-1/2}=1$. For the σ_+ light tuned to the $D1$ transition, the optical-pumping-rate equations are

$$\frac{d\rho_{\pm1/2}}{dt}=\pm\left[\frac{\Gamma_{SD}}{2}+\gamma_{opt}\right]\rho_{-1/2}\mp\frac{\Gamma_{SD}}{2}\rho_{+1/2}\ , \tag{1}$$

where Γ_{SD} is the total bulk spin destruction rate, and γ_{opt} is the optical-pumping (photon scattering) rate per Rb atom defined by

$$\gamma_{opt}(\vec{r})=\int\Phi(\vec{r},\nu)\sigma(\nu)d\nu\ , \tag{2}$$

where $\Phi(\vec{r},\nu)=dI(\vec{r})/d\nu$ is the laser intensity per unit frequency, which is in general position dependent, and $\sigma(\nu)$ is the optical-absorption cross section at the laser frequency ν. $\Phi(\vec{r},\nu)$ is related to the light intensity I and total laser power P by $I(\vec{r})=\int\Phi(\vec{r},\nu)d\nu$ and $P(\vec{r})=\int d^2r\int h\nu\Phi(\vec{r},\nu)d\nu$. The cross section is assumed to have a Lorentzian line shape with a linewidth Γ, i.e.,

$$\sigma(\nu)=\frac{\sigma_0}{1+4(\nu-\nu_0)^2/\Gamma^2}\ . \tag{3}$$

In practice, this is dominated by pressure broadening (18 GHz/atm for ^{3}He and 14 GHz/atm for N_2 [19]), which greatly exceeds the natural (5.7 MHz) and Doppler (250 MHz at 200°C) widths. The far wings of the line are actually broadened asymmetrically due to the nature of the alkali-metal–buffer-gas collision interaction [20]. This will be important for the detailed modeling of the frequency dependence of optical pumping discussed in Sec. III.)

The peak absorption cross section can be calculated from the sum rule

$$\int\sigma(\nu)d\nu=\pi r_e c f\ , \tag{4}$$

where r_e is the classical electron radius, c is the speed of light, and f is the transition oscillator strength. The absorption rate scales inversely with Γ (i.e., cell pressure). The peak cross section is 3.2×10^{-13} cm^2 for $\Gamma_{at}=18$ GHz. Diffusion effects, considered in Sec. III, have been neglected in Eq. (1).

Assuming an initially unpolarized vapor, the solution to Eq. (1) is

$$P_{Rb}(\vec{r},t)=(\rho_{+1/2}-\rho_{-1/2})$$
$$=\frac{\gamma_{opt}(\vec{r})}{\gamma_{opt}(\vec{r})+\Gamma_{SD}}(1-e^{-[\gamma_{opt}(\vec{r})+\Gamma_{SD}]t})\ . \tag{5}$$

As noted above, the steady-state polarization is deter-

mined by an equilibrium between photon absorption and spin destruction. The time dependence in Eq. (5) is characterized by $\gamma_{\rm opt}\approx\Phi(\nu_0)\sigma(\nu_0)$, which is typically 400 Hz per mW/cm^2.

B. The role of nuclear spin: slowing factors

All of the stable alkali-metal atoms have nonzero nuclear spin. In the case of Rb, two isotopes exist, ^{85}Rb and ^{87}Rb, with nuclear spins $I=\frac{5}{2}$ and $\frac{3}{2}$, respectively. The natural abundances of these isotopes are approximately 72% and 28%, respectively. The ground and excited states of the $D1$ transition contain two hyperfine multiplets, $F=I+\frac{1}{2}$ and $F=I-\frac{1}{2}$, and the ground states consist of 12 and eight levels, respectively. For the excited state, p-state mixing and quenching collisions dominate, and therefore each ground state is repopulated with equal probability.

A circularly polarized photon can induce any of the possible transitions satisfying the selection rule $\Delta m_F=+1$, and the relevant Clebsch-Gordan coefficients for these processes must be taken into account in the optical-pumping-rate equations. For a sample of natural Rb, there are a total of 20 optical-pumping-rate equations. Similar to Eq. (1), these consist of optical pumping and electron randomization terms. They can be written [12]

$$\left[\frac{d\rho_{Fm}}{dt}\right]_{\rm OP}=-\alpha_{Fm}\rho_{Fm}+\frac{1}{2(2I+1)}\sum_{F',m'}\alpha_{F'm'}\rho_{F'm'} \quad (6)$$

and

$$\left[\frac{d\rho_{Fm}}{dt}\right]_{\rm ER}=-\tfrac{3}{4}\Gamma_{\rm ER}\rho_{Fm}+\Gamma_{\rm ER}\langle Fm|\mathbf{S}\cdot\rho\mathbf{S}|Fm\rangle\ , \quad (7)$$

where $\mathbf{S}$ is the electron spin, ρ_{FM} and α_{Fm} are the population density and absorption coefficient of the F,m sublevel, and $\Gamma_{\rm ER}$ is the electron randomization rate. The term electron randomization is used to denote the electronic nature of the relaxation process, as is evident from the matrix elements in Eq. (7). This occurs because the time scale of the collision ($\tau_c\approx 1$ Å$/v_{\rm rms}\approx 10^{-12}$ s) is much shorter than the hyperfine interaction time. Therefore, during the collision the electron is effectively decoupled from the nucleus and only the electron spin can flip. It is only during the relatively long periods between collisions that the hyperfine coupling of the nuclear spin to the electron spin leads to partial decay of the nuclear polarization.

We define the hyperfine polarization (P_F) and the electron-spin polarization (P_S) as

$$\begin{aligned}P_F&=\frac{\sum_{F,m} m\rho_{Fm}}{\sum_{F,m}\rho_{Fm}}=\langle F_z\rangle\ ,\\ P_S&=\frac{1}{2I+1}(P_{I+1/2}-P_{I-1/2})=\langle S_z\rangle\ ,\end{aligned} \quad (8)$$

where $P_{I+1/2}$ and $P_{I-1/2}$ are the polarizations in the upper and lower hyperfine multiplets, respectively. The sum in P_F includes all values of F and m. (For convenience, we define the electron polarization as $P_s=\langle S_z\rangle=P_{\rm Rb}/2$.)

The effect of the nuclear spin is to slow the spin-relaxation processes: The nucleus acts as a reservoir of angular momentum and the relaxation process must draw spin from the atom (electron plus nucleus) via the hyperfine coupling of the nucleus to the electron spin. Similarly, optical pumping is slowed because the total spin of the atom must be polarized: i.e., each photon provides only one unit of angular momentum, while the atom with nonzero nuclear spin requires many units of angular momentum to optically pump into the $m=+F$ state.

Spin exchange between Rb atoms leads to equilibration of electronic spin for both isotopes. Gibbs and Hull [21] have measured the ^{87}Rb-^{87}Rb spin-exchange rate constant to be 7.9×10^{-10} cm^3/s, yielding rates on the order of 10^5 s^{-1} for Rb densities of approximately 10^{14} cm^{-3}. Assuming a comparable rate for ^{85}Rb and for ^{85}Rb-^{87}Rb spin exchange, this process should dominate all others in the vapor. Anderson, Pipkin, and Baird [22] have shown that under these conditions the polarization can be described by a single parameter, the spin temperature, and the density matrix can be written

$$\rho_{Fm}=N(\beta)e^{\beta m}\ , \quad (9)$$

where $N(\beta)$ is a normalization constant, and β is the spin temperature. Qualitatively, Eq. (9) states that rapid spin exchange establishes a Boltzmann distribution of the hyperfine levels consistent with the total polarization (since spin exchange is a spin-conserving interaction).

Assuming a distribution of populations of the hyperfine magnetic sublevels given by a spin temperature β^{-1}, we define the nuclear slowing factor

$$S=\frac{P_F}{P_S}\ , \quad (10)$$

where the hyperfine polarization (P_F) and electron polarization (P_S) for ^{85}Rb ($F=2$ and 3) and ^{87}Rb ($F=1$ and 2) are

$$\begin{aligned}P_F(^{85}\mathrm{Rb})&=\frac{(6\sinh3\beta+8\sinh2\beta+4\sinh\beta)}{\sum_{F,m}\exp(\beta m)}\ ,\\ P_F(^{87}\mathrm{Rb})&=\frac{(4\sinh2\beta+4\sinh\beta)}{\sum_{F,m}\exp(\beta m)}\ ,\\ P_S(^{85}\mathrm{Rb})&=\frac{\sinh3\beta}{\sum_{F,m}\exp(\beta m)}\ ,\\ P_S(^{87}\mathrm{Rb})&=\frac{\sinh2\beta}{\sum_{F,m}\exp(\beta m)}\ ,\end{aligned} \quad (11)$$

where the sums span F and m for each isotope. For natural Rb these polarizations are weighted by the isotopic abundances:

$$P_F(\mathrm{Rb})=0.28N_3(\beta)(4\sinh 2\beta+4\sinh\beta)+0.72N_5(\beta)(6\sinh 3\beta+8\sinh 2\beta+4\sinh\beta)\ ,$$
$$P_S(\mathrm{Rb})=0.28N_3(\beta)\sinh 2\beta+0.72N_5(\beta)\sinh 3\beta\ , \tag{12}$$

where $N_3(\beta)$ and $N_5(\beta)$ are the normalization factors for the $\frac{3}{2}$ and $\frac{5}{2}$ species, respectively. S varies from 5.44 for high polarization ($\beta\rightarrow\infty$) to 10.8 ($\beta\rightarrow 0$) for zero Rb polarization. Figure 2 illustrates the slowing factor as a function of the electron polarization for natural Rb.

Equation (7) can then be written

$$\frac{dP_F}{dt}=-\frac{\Gamma}{S}P_F\ , \tag{13}$$

which is not truly exponential since S, the factor by which the electron polarization decay is slowed, depends on the polarizations. The electron polarization buildup is also slowed by the factor S, so that the time dependence of optical pumping is given by

$$P_{\mathrm{Rb}}(t)=\frac{\gamma_{\mathrm{opt}}}{\gamma_{\mathrm{opt}}+\Gamma_{\mathrm{SD}}}(1-e^{-[(\gamma_{\mathrm{opt}}+\Gamma_{\mathrm{SD}})/S]t})\ . \tag{14}$$

As expected, the equilibrium polarization is not changed; only the time dependence changes, and the time dependence is nonexponential.

C. Polarization in a high-density vapor

The condition of an optically thin vapor, assumed up to this point, provides that the same constant photon flux $\Phi(\nu)$ irradiates each atom in the vapor. We now consider the case of an optically thick vapor. This is characterized by the inequality

$$[\mathrm{Rb}]\sigma_0 l\gg 1\ , \tag{15}$$

where $\sigma_0=\sigma(\nu_0)$ is the on-resonant absorption cross section previously introduced, and l is the sample length along the laser beam direction $\hat{z}$. The photon flux in this case varies with z:

$$\frac{d\Phi(\nu,\vec{r})}{dz}=-\lambda^{-1}(\nu,\vec{r})\Phi(\nu,\vec{r})\ , \tag{16}$$

where $\lambda(\nu,\vec{r})$ is the (position dependent) absorption length given by

$$\lambda^{-1}(\nu,z)=3[\mathrm{Rb}]\sigma(\nu)(|\langle\tfrac{1}{2},-\tfrac{1}{2},1,m_p|\tfrac{1}{2},m\rangle|^2\rho_{-1/2}+|\langle\tfrac{1}{2},+\tfrac{1}{2},1,m_p|\tfrac{1}{2},m\rangle|^2\rho_{+1/2}) \tag{17}$$

where $m_p=0,\pm 1$ is the z projection of the incident photon angular momentum, and m is the value of m_s in the excited state after photon excitation. For unpolarized light incident ($m_p=0$) on an unpolarized sample, both Clebsch-Gordon coefficients are equal to $\frac{1}{3}$ and the states are equally populated, giving a constant absorption coefficient $\lambda_0^{-1}(\nu)=[\mathrm{Rb}]\sigma(\nu)$. For σ_+ light incident on a polarized vapor, however, the absorption is polarization dependent according to

$$\lambda^{-1}(\nu,\vec{r})=2[\mathrm{Rb}]\sigma(\nu)\rho_{-1/2}(\vec{r})=[\mathrm{Rb}]\sigma(\nu)[1-P_{\mathrm{Rb}}(\vec{r})]\ , \tag{18}$$

with the position dependence of the polarization following from the attenuation of the optical-pumping rate derived by combining Eqs. (18) and (2).

III. DIFFUSION-DRIVEN RB POLARIZATION GRADIENTS

Wall relaxation of Rb polarization is driven by diffusion, and is accounted for in Eq. (1) (including the nuclear-spin slowing factor S) by adding the term $D\nabla^2\rho$:

$$\frac{d\rho_{\pm 1/2}}{dt}=\pm\frac{1}{S}\left[\frac{\Gamma_{\mathrm{SD}}}{2}+\gamma_{\mathrm{opt}}\right]\rho_{-1/2}\mp\frac{1}{S}\frac{\Gamma_{\mathrm{SD}}}{2}\rho_{+1/2}+D\nabla^2\rho_{\pm 1/2}\ , \tag{19}$$

where D is the Rb diffusion constant. The slowing of the electron randomization processes and the optical-pumping rate caused by the nuclear spin is not included in the diffusion term because, in contrast to electron randomization rates, wall relaxation occurs on a time scale long compared to the hyperfine precession period, i.e., the atom resides near the wall for much longer than 1 ns. Therefore, the entire spin of the atom is destroyed during each wall collision.

In general it is most useful to solve Eq. (19) numerically; however, it is illustrative to explore an analytic solution in one dimension that neglects the effects of radial diffusion. We follow the method developed by Gornyi

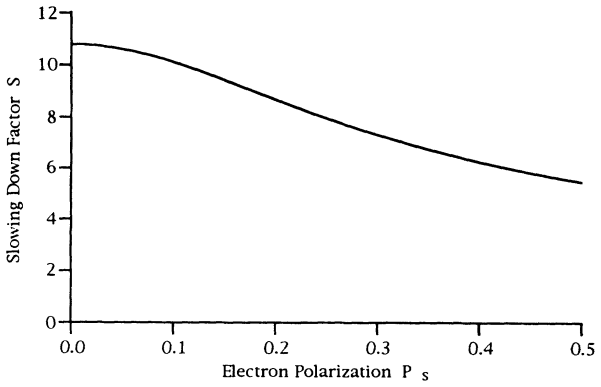

FIG. 2. The slowing factor due to the Rb nuclear spin for natural Rb plotted as a function of electron polarization.

and Matisov [23], and consider the polarization in steady state by setting $d\rho_{\pm 1/2}/dt=0$.

We define a propagation parameter $\Psi(\tau)$ by

$$\Phi(\tau,\nu)=\Phi(0,\nu)e^{-\beta(\nu)\Psi(\tau)}, \tag{20}$$

where $\tau=z/\lambda_0$, and $\beta(\nu)$ is the atomic line-shape function. Using Eqs. (16) and (18), we find that $\Psi(\tau)$ satisfies

$$\frac{d\Psi(\tau)}{d\tau}=1-P(\tau). \tag{21}$$

Substituting and integrating over τ, we find

$$\lambda_0^{-2}D\frac{d^2\Psi(\tau)}{d\tau^2}+\frac{\Gamma_{SD}}{S}[\tau-\Psi(\tau)]+\frac{\Phi(0)\sigma_0}{S}e^{-\beta(\nu_L)\Psi(\tau)}=C, \tag{22}$$

where C is an integration constant determined by the boundary conditions $\Psi(0)=0$ and $\Psi'(0)=\Psi'(l)=1$. For simplicity, we assume a narrow-band laser at frequency ν_L.

We first consider the limit of high Rb polarization, and an optically thin cell. In this limit γ_{opt} is constant. We further assume no radial dependence of the laser intensity or polarization, and that $S=5.44$ is constant. Equation (22) thus simplified is linear and satisfied by the solution

$$P(z)=\frac{\gamma_{opt}(0)}{\gamma_{opt}(0)+\Gamma_{SD}}\left[1-\frac{e^{-z/l_D}+e^{-(l-z)/l_D}}{1+e^{-l/l_D}}\right], \tag{23}$$

where l_D is given by

$$l_D=\left[\frac{5.44D}{\gamma_{opt}(0)+\Gamma_{SD}}\right]^{1/2}. \tag{24}$$

The polarization at the front of the cell can be found in the approximation $z\ll l$ and $l_D\ll l$, in which case

$$P(z)=1-e^{-z/l_D}. \tag{25}$$

This shows that $P(z)$ rises over a characteristic length l_D in the limit $l_D\ll\lambda_0$, i.e., $\gamma_{opt}(0)$ is effectively constant over the distance l_D. Here $\lambda(\nu_0)=[\mathrm{Rb}]\sigma(\nu_0)$ is the absorption length for resonant light. This behavior is closely related to the orientation confinement produced by a buffer gas, first introduced by Masnou-Seeuws and Bouchiat [24].

In Eq. (23), the polarization in the bulk is a constant because of the assumption of negligible absorption except in the vicinity of the walls. In fact, this solution is valid as long as the incident power is sufficient to satisfy

$$\gamma_{opt}(0)\gg\frac{10.8D}{\lambda_0^2}, \tag{26}$$

so that the diffusion layer is small compared to the optical thickness for the largest possible value of S (10.8). This is no longer the case further into the cell, where the light intensity has dropped significantly. As an example, at a Rb density of 5×10^{14} cm^3, assuming a typical diffusion constant of $D=0.3$ cm^2/s, 200–300 mW/cm^2 is required to satisfy this inequality at the front window.

A. Numerical calculations

Practical cases of diffusion effects can most conveniently be solved numerically. We begin by considering the steady state: the Rb polarization $P(\vec{r})$ satisfies the diffusion equation

$$D\nabla^2P(\vec{r})-\frac{\Gamma_{SD}}{S(\vec{r})}P(\vec{r})+\frac{\gamma_{opt}(\vec{r})}{S(\vec{r})}[1-P(\vec{r})]=0. \tag{27}$$

Here D, Γ_{SD}, and γ_{opt} are the diffusion constant, bulk spin destruction rate, and optical-pumping rate defined above. The slowing factor $S(\vec{r})$ depends on the Rb vapor polarization and therefore on position. The laser light is incident along the z axis of a cylindrical cell of length l and radius a, and we assume that the laser beam is cylindrically symmetric. The position dependence of $\Phi(r,z,\nu)$ is given by

$$\frac{d\Phi(r,z,\nu)}{dz}=-[\mathrm{Rb}]\sigma(\nu)[1-P(r,z)]\Phi(r,z,\nu). \tag{28}$$

These equations have been solved by relaxation methods in two dimensions assuming cylindrical symmetry of the cell walls and incident light, and with the boundary conditions for the polarization at the cell wall $P(r,0)=P(r,l)=P(a,z)=0$. (i.e., the total spin of the atom F_z is destroyed by each wall collision). The measurements described below support this assumption for cells with no wall coatings. Wall coatings have been used to reduce sticking times [25], and will be considered in future work.

The influence of the layer of unpolarized Rb is a sharp decrease in laser intensity in the vicinity of the front cell wall. When the inequality $l_D\ll\lambda_0$ is not satisfied, the laser intensity varies across the boundary layer and the polarization rises over a distance nl_D, where $n\geq1$ (where $n=1$ defines the limit of an optically thin vapor). Under these conditions, a significant fraction of the incident laser light may be absorbed by the layer of unpolarized Rb vapor. This effect is, of course, greatest on resonance where the absorption length of the light is shortest and leads to the dip structure shown in Fig. 1. This dip structure should become apparent when the laser intensity at the end of the cell ($z=l$) is reduced, so that $\gamma_{opt}(l)$ is of the order of Γ_{SD}; that is, when

$$\gamma_{opt}(0)e^{-nl_D/\lambda_0}\ll\Gamma_{SD}\frac{l}{\lambda_0}. \tag{29}$$

In the comparison of the calculations with measurements described below, we use three variables to investigate the resonant decrease of Rb polarization: the Rb number density which affects λ_0 and Γ_{SD}, the laser intensity which affects γ_{opt}, and the buffer-gas pressure which affects D and $\sigma(\nu)$ (via the pressure-broadened atomic linewidth). Both D and γ_{opt} are inversely proportional to the buffer-gas pressure, and since $\gamma_{opt}(0)\gg\Gamma_{SD}$ in all practical situations, l_D is approximately independent of the buffer-gas pressure. We illustrate this with calculations of the polarization distributions in an optically pumped Rb vapor under the experimental conditions chosen for these studies. The dip structure illustrated in

Fig. 1 should be most sensitive to wall relaxation effects, and essentially insensitive to other details of the optical-pumping process such as spin destruction.

B. Measurements of diffusion effects

In order to test our calculations, we have performed measurements of the vapor polarization as a function of laser wavelength. The experimental setup is shown in Fig. 3. The three main elements of the setup are the titanium:sapphire laser used to polarize the vapor, the diode laser system for probing the polarization, and the cell in which the compositions and densities of buffer gases could be varied.

A special teflon-seal valved cell was used for these measurements in order to facilitate the refilling of the same cell with different buffer gases [26]. By using the same cell for Rb density and polarization measurements, an accurate and reproducible measure of the Rb number density could be made. Because Teflon reacts with Rb metal, a number of precautions were taken to ensure that the Rb stayed in the experimental region of the cell and out of the neck. For ^{3}He the cell pressure was seen to drop as much as 2–3 % per day at pressures above 3 atm. For N_2, the cell maintained the gas pressure with negligible loss for many weeks. For this reason, we used only N_2 as a buffer gas in most of the experiments. The Rb density in optical pumping cells has often been assumed on the basis of equilibrium vapor pressure curves (e.g., Ref. [27]), but we have observed variations by factors of 2 or more even when great care was taken to produce uniform temperatures throughout the cell. It is also well known that a cell must be heated for many days in order for it to cure [13]. We therefore measured the Rb density in the cell by Faraday rotation [28]. Rb density was found to be reproducible to 5% as measured by Faraday rotation, and demonstrated by the consistency of several independent measurements.

A Ti:sapphire laser with variable power up to 5 W was used. Scanning of the Ti:sapphire laser wavelength was accomplished with a motorized micrometer. The laser wavelength could be scanned over a range of approximately 30–40 Å with a reproducibility of ±0.3 Å. The laser was found to scan linearly over most of the scanning range except at a few positions where it would skip by 0.25–0.5 Å. These positions could be changed by retuning the laser cavity, but for a given tuning of the cavity the mode hops occurred at well-defined and reproducible wavelength positions. The quality of the pump circular polarization was typically 95% or better.

The Rb polarization was detected by a weak probe from a 3-mW $Ga_{1-x}Al_xAs$ diode laser operated near the $D2$ resonance. The probe beam polarization was modulated with a photoelastic modulator (PEM). As pointed out by Bouchiat and Brossel [29], the populations of the Rb levels can be expressed as polarization moments including the dipole polarization $\langle F_z \rangle$, the quadrupole polarization $\langle 3F_z^2 - \mathbf{F}\cdot\mathbf{F} \rangle$, and the hyperfine population imbalance $\langle \mathbf{S}\cdot\mathbf{I} \rangle$. The particular combination of these moments depends on the polarization of the light. For complete circularly polarized light, only the dipole polarization $\langle F_z \rangle$ is measured. The modulation of the probe beam by the PEM insures that the light is circularly polarized at some time during the cycle of modulation as shown in Fig. 4. The transmission of polarization modulated probe beam through the Rb vapor is given by

$$I(l)=I(0)\exp\left[-[\mathrm{Rb}]\sigma(\nu_L)l\left[1+\frac{\bar{P}_{\mathrm{Rb}}}{2}\sin(\pi\sin\omega t)\right]\right], \tag{30}$$

where $\bar{P}_{\mathrm{Rb}}$ is the average dipole (vector) polarization of the Rb vapor measured along the probe beam, and ω is the PEM oscillation frequency. At the extrema of the transmission, the probe light is either σ_+ or σ_-, and we therefore have an unambiguous measure of the spin polarization of the vapor.

C. Results and comparison of data and numerical simulations

Experiments were carried out using only N_2 buffer gas because the valved cell leaked at high ^{3}He gas pressures.

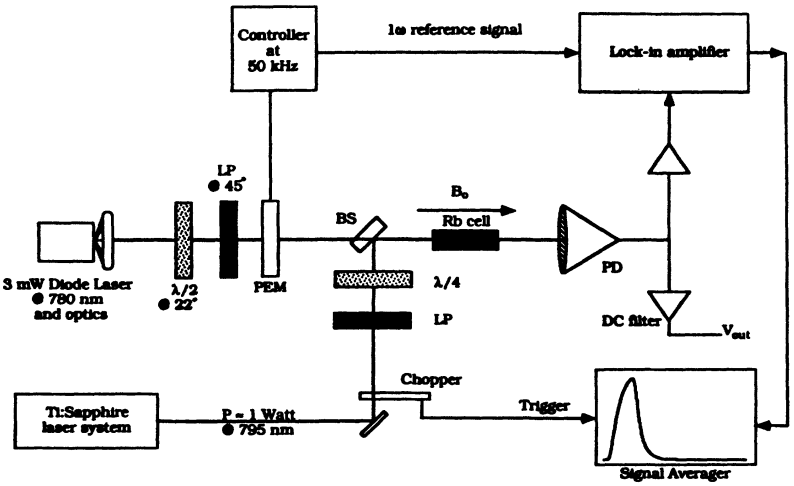

FIG. 3. Schematic view of the apparatus used for measurements of laser-tuning dependence of Rb polarization and Rb spin destruction rates. PD denotes a photodiode, LP is a linear polarizer, and PEM is a photoelastic modulator.

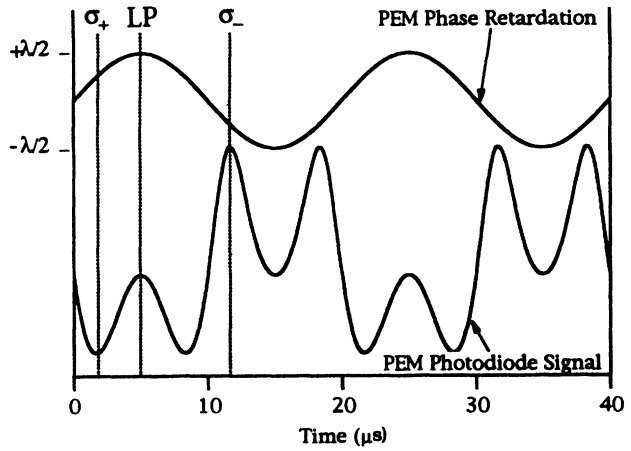

FIG. 4. Plot of the PEM phase retardation and its effect on the transmission of the $D2$ probe beam through a polarized vapor.

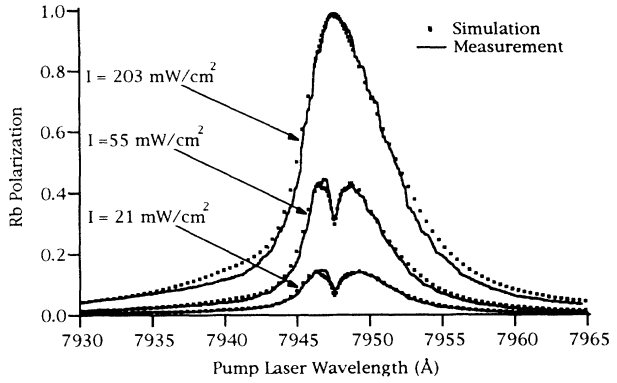

FIG. 5. Polarization plots for [Rb] = 3.0×10^{14} cm^3 and $I_{in}=21$, 55, and 203 mW/cm^2. N_2 pressure is 1142 torr.

A second reason for using only N_2 buffer gas was the possibility of larger errors in the estimation of the Rb-^{3}He contribution to the spin destruction rate, an important fixed parameter in the calculations (see discussion in Sec. V). Measurements were performed for three values of N_2 pressure: $P_{N_2}=397$, 1142, and 3090 torr. The important experimental parameters for these three cases are listed in Table I.

A two-dimensional-relaxation computer code was written to calculate the expected polarization vs laser wavelength line shapes for Rb densities varying from approximately 1×10^{14} to 7×10^{14}/cm^3, and laser intensities varying between 10 and 1000 mW/cm^2. By looking at the wavelength dependence of the optical pumping, we were able to obtain the maximum amount of information from the data and calculations: the width of the polarization line shape gives the power broadening of the optical pumping polarization line shape [17], the maximum polarization contains information about the Rb density and the total spin destruction rate, and the resonant decrease in optical pumping efficiency characterizes the effects of diffusion and wall relaxation.

Figure 5 shows data and the result of the calculation for P_{Rb} vs λ for a N_2 pressure of 1142 torr. The Rb density is 3.0×10^{14}/cm^3, and the incident laser intensity is set at 21, 55, and 203 mW/cm^2. The asymmetry in the polarization line shapes seen here is due to the asymmetric line broadening. The line shape is parametrized by [20]

$$\beta(\nu)=\frac{1}{1+4(\nu-\nu_0)^2/\Gamma^2}+a(\nu-\nu_0)e^{-|\nu-\nu_0|/\Gamma_{as}}. \quad (31)$$

The asymmetry parameters, a and Γ_{as}, were found by fitting the Rb absorption line shape with the above function. The resulting values can be found in Table I. Further comparison of experiment and theory for the wavelength dependence of Rb polarization are shown in Figs. 6, 7, and 8 for the values of buffer-gas pressure, Rb density, and intensity levels shown. Overlaid on the plots are the calculations; qualitatively, the agreement is seen to be excellent. The only free parameter in the calculations was the laser intensity, since the actual intensity incident on the vapor was not known. All other parameters were measured and fixed in the calculations (i.e., [Rb], σ_0, Γ_{SD}, D, Γ, a, and Γ_{as}). There are a number of possible reasons for variations in the pump intensity. First, reflection losses at the cell and oven windows and those due to condensed Rb on the front window were not well known. Second, the diode laser beam only probed a narrow portion of the vapor cell, whereas the pump beam was expanded to fill the entire radius of the cell. Therefore, slight misalignments of the pump beam could cause greater than 10% variations in the incident pump intensity along the probe beam. Finally, power adjustment of the pump was accomplished by changing the Ar^+ ion laser pump power. This could lead to small changes in the lasing characteristics of the Ti:sapphire laser such as the Gaussian beam radius. This too would lead to changes in the incident optical-pumping intensity. The laser intensity used in the calculation was adjusted by small amounts from its expected value (using the Gauss-

TABLE I. Relevant experimental parameters for the three polarization data sets, where P_{N_2} is the N_2 pressure, Γ is the Rb atomic linewidth, D is the Rb diffusion constant, σ_0 is the peak $D1$ absorption cross section, a and Γ_{as} are the asymmetry parameters, and $\Gamma_{SD}^{N_2}$ is the nitrogen contribution to the Rb spin destruction rate.

P_{N_2} (torr)	Γ (GHz)	D (cm^2/s)	σ_0 (10^{-13} cm^2)	a (GHz^{-1})	Γ_{as} (GHz)	$\Gamma_{SD}^{N_2}$ (Hz)
397	7.0	0.52	8.13	1.6×10^{-5}	63	119
1142	20.3	0.18	2.82	1.6×10^{-4}	63	343
3090	54.5	0.067	1.04	1.2×10^{-3}	63	927

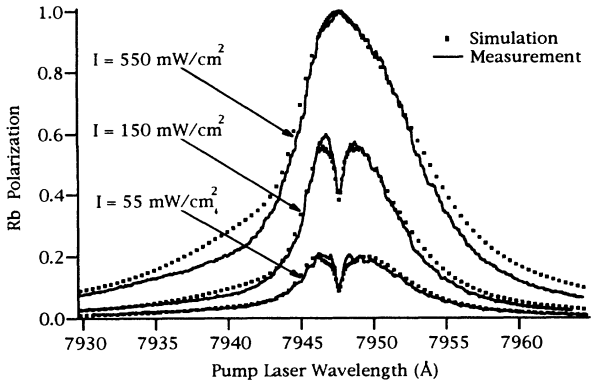

FIG. 6. Polarization plots for [Rb] = 4.7×10^{14} cm^3 and $I_{in}=55$, 150, and 550 mW/cm^2. N_2 pressure is 1142 torr.

ian beam radius measured at high power and an estimate of the power losses at the glass interfaces) until the value of the maximum polarization obtained off-resonance matched the measured value. Typical losses were 10–15 %.

The good agreement of the power-broadened polarization widths for most cases would seem to indicate that the correct intensities were used in the calculations. However, at high pump powers the agreement for the power-broadened widths becomes increasingly poor. Comparison between the three different P_{N_2} data sets shows that the power-broadened widths become increasingly narrower than expected with decreasing N_2 pressure and increasing pump intensity. With a buffer-gas pressure of 3090 torr, for example, the agreement in width is very good for intensities up to 300 mW/cm^2, whereas for 84 mW/cm^2 and a pressure of 397 torr the calculated and measured widths are not in good apparent agreement. The pressure dependence suggests that the effect may in some way be related to diffusion. One possibility is radial diffusion, which is only approximated by our two-dimensional calculations. This creates a boundary layer in the radial direction which is dependent on the optical-pumping rate near the radial wall. In contrast to axial diffusion, this is not a resonant phenomenon and could affect the polarization in the far wings. In fact, in the far wings the optical-pumping rates are small, leading to large radial boundary layer thicknesses which may

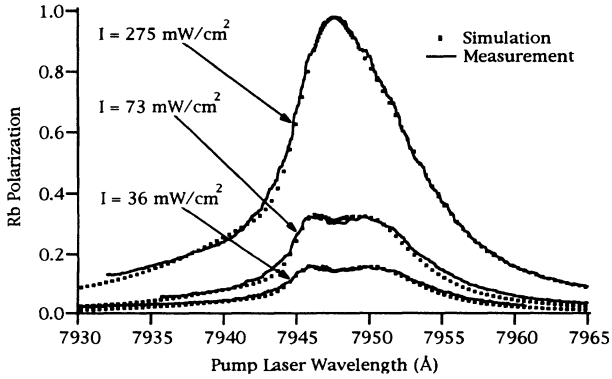

FIG. 7. Polarization plots for [Rb] = 2.5×10^{14} cm^3 and $I_{in}=36$, 73, and 275 mW/cm^2. N_2 pressure is 3090 torr.

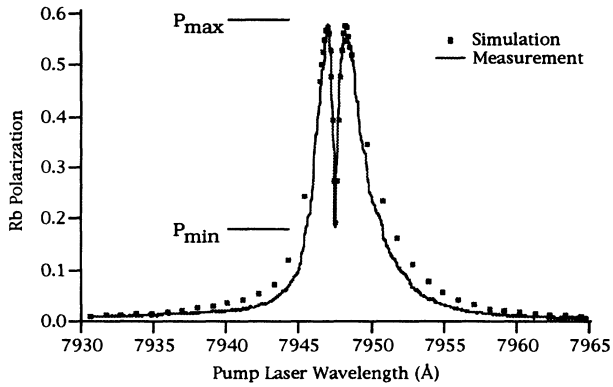

FIG. 8. Polarization plots for [Rb] = 4.0×10^{14} cm^3 and $I_{in}=84$ mW/cm^2. N_2 pressure is 397 torr.

even affect the polarization near the cell axis. However, both one-dimensional calculations which neglect radial diffusion, and two-dimensional calculations which approximate the effects of radial diffusion, produced the same widths for the polarization line shapes. Therefore, it is unlikely that radial diffusion is the answer. A second possibility is added spin destruction mechanisms due to high pump powers for which we have not accounted. Such an effect is worthy of further investigation, but since we are most concerned with on- and near-resonant polarization this possibility is not pursued further in this paper.

For the lower pressure case shown in Fig. 8 (397-torr N_2), the atomic linewidth is 7 GHz and the linewidth of the pump laser is several GHz. We have therefore incorporated a finite laser linewidth into the calculation by assuming a spectral distribution given by a Lorentzian. We use this smooth line shape instead of one consisting of many discrete cavity modes because the homogeneously broadened Rb absorption line averages over many modes of the laser cavity. We have been able to obtain excellent agreement with theory for this entire data set with a laser line width of 8 GHz. We have measured the Ti:sapphire width to be about 3 GHz, but it is possible that the mode structure fluctuates on a very short time scale ($\lesssim 10$ ms) unobservable with our diagnostics (an 8-GHz free spectral range Fabry-Perot). A comparison of calculation and data is shown in Fig. 8. The narrow laser line calculation predicts $P_{Rb}=0.018$ at line center.

In Fig. 9, we show the calculated "dip ratio," P_{min}/P_{max} (as indicated in Fig. 8), as a function of l_D/λ_0. The solid lines are fits of the results for calculations at discrete points to the functional form,

$$\frac{P_{min}}{P_{max}} \propto e^{-nl_D/\lambda_0} . \tag{32}$$

where we define nl_D as an effective boundary layer thickness, and n is a free parameter in the fit. The decay constants n for 397, 1142, and 3090 torr are 6.90, 1.41, and 1.17, respectively. These numbers precisely set the scale for characterizing the absorption within the layer. In the first case, $n \gg 1$, indicating that absorption occurs within a region much larger than our naive estimate of the boundary layer. This is because the large absorption

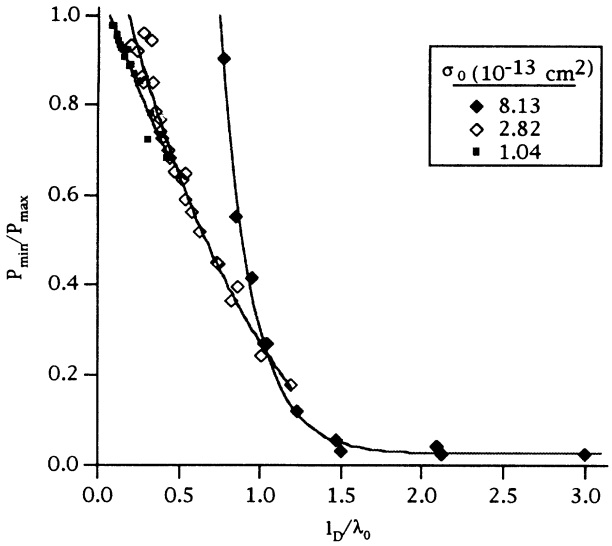

FIG. 9. Calculations of the ratio of on-resonant polarization to maximum polarization achieved off-resonance as a function of l_D/λ_0 for the absorption cross sections indicated. The solid lines are fits to the calculation that assume the exponential decrease of the polarization within the layer given by Eq. (32) with values of n of 6.90, 1.41, and 1.17, respectively, for $\sigma_0 = 8.1$, 2.8, and 1.0×10^{-13} cm^2, respectively.

cross section leads to a significant attenuation of laser intensity, effectively increasing the thickness of the absorbing layer (i.e., a much larger length is required for the polarization to grow to its maximum value). At higher buffer-gas pressures, only moderate absorption occurs within the boundary layer, so that the layer thickness is

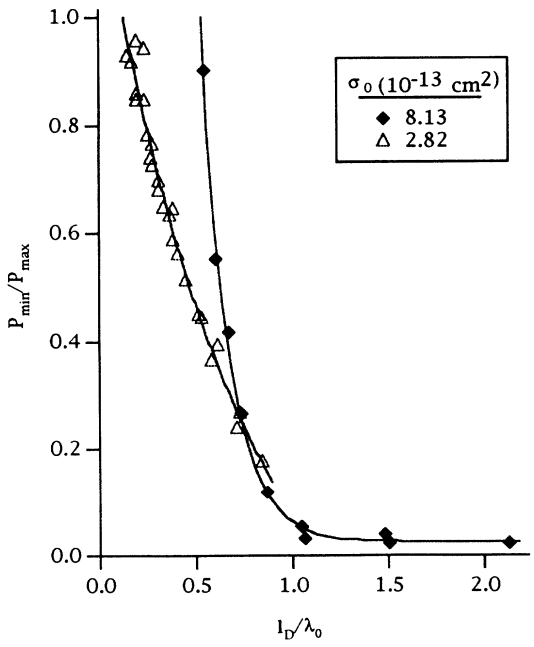

FIG. 10. Experimentally determined "dip ratio" as a function of l_D/λ_0. Solid lines are the fits to numerical calculations assuming 8-GHz laser linewidth. Data are shown for absorption cross sections $\sigma_0 = 8.1$ and 2.8×10^{-13} cm^2. The solid lines are from Fig. 9.

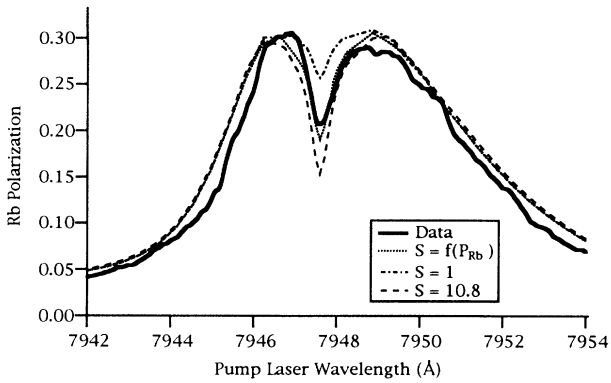

FIG. 11. Comparison of polarization calculations with data for various assumptions for the slowing effect of nuclear spin.

not as strongly affected by absorption. At still higher pressures the average polarization within the absorbing layer is significantly greater than zero. In Fig. 10 the experimental values of P_{min}/P_{max} are plotted along with the fits to the model of Eq. (32).

To put these comparisons in perspective, we have plotted in Fig. 11 a typical data set illustrating the resonant dip structure along with three possible model calculations. One is the model developed up to this point with the nuclear-spin-slowing effects derived from Eqs. (12). The two other models make different assumptions about the relative slowing of wall relaxation with respect to the optical-pumping and spin destruction processes. For $S = 1$, the slowing effects of the nuclear spin are neglected, as would be the case if wall collisions only partially destroy the total Rb polarization. For the second calculation, the slowing factor was assumed to take on its low polarization value of 10.8. In both cases, the agreement between experiment and theory is poor, supporting the model's validity that S is a function of P_{Rb}.

In this section, we have introduced methods for calculating spatial polarization profiles in dense alkali-metal vapors via numerical techniques. The procedure has only been applied here to the two-dimensional case of a cylindrical cell irradiated by a Gaussian beam of resonant or off-resonant radiation, but it is easily extended to the general three-dimensional case. This analysis has led to the characterization of a marked resonant decrease in polarization which becomes manifest at high vapor densities and low incident intensity levels. Experiments have also been presented which show good agreement with the theoretical calculations over a large range of the relevant variable experimental parameters.

IV. MEASUREMENT OF COLLISIONAL RELAXATION OF RB POLARIZATION

Spin-relaxation rates constants are the crucial input data for the calculations described in Sec. III, and we have remeasured those for Rb-Rb, Rb-^{3}He, and Rb-N_2 collisions. In these collisions, the electron spin is randomized, leading to complete depolarization. In practice, we measure the time dependence of the Rb polarization, which is due to all spin destruction processes including

collisions and wall relaxation. In the steady state, wall relaxation is manifest in the polarization gradients and the dip structure; however, in the transient measurements described here, we formulate wall relaxation in terms of diffusion modes.

Spin destruction can be depicted by the general (schematic) equation

$$A(\uparrow)+B\rightarrow A(\downarrow)+B\ , \tag{33}$$

where A is the alkali-metal atom of interest, and B is some foreign atom. For the cases to be considered, B is either another alkali-metal atom, a buffer-gas atom, or the cell wall (more specifically, an impurity ion embedded in the cell wall). The missing angular momentum is taken up by the external degrees of freedom of the collision pair during the collision.

All spin-destroying collisions are due to spin-spin and spin-rotation interactions. The spin-spin interaction between an alkali-metal atom and paramagnetic impurities in the glass walls are most likely responsible for wall relaxation. Also, there is a strong spin-spin force during a collision between two polarized alkali-metal atoms, which is most likely the cause of Rb-Rb spin destruction. In the case of buffer-gas collisions, however, because the gases are not paramagnetic, spin rotation is the dominant relaxation mechanism. The fact that spin rotation leads to spin relaxation can be described semiclassically as due to precession of the electron spin about the total angular momentum vector during the duration of the collision. After the collision, the electron spin has a smaller projection along the initial quantization axis. A similar argument can be used to explain relaxation in spin-spin collisions.

Spin relaxation of a polarized Rb sample is given by Eq. (27) with $\gamma_{\rm opt}=0$:

$$\frac{\partial P}{\partial t}=D\nabla^2 P-\frac{\Gamma_{\rm SD}}{S}P\ . \tag{34}$$

Assuming the boundary condition $P_{\rm Rb}=0$ at the cell walls, this can be solved analytically in two dimensions for a cylindrical cell of length l and radius a by expanding the polarization in cylindrical coordinates [30]:

$$P(z,r,t)=\sum_{m,n}A_{mn}J_0\left[\mu_m\frac{r}{a}\right]\sin\left[\frac{n\pi}{l}z\right]e^{-\Gamma_{mn}t}\ , \tag{35}$$

where A_{mn} are normalization constants chosen to produce the initial polarization distribution $P(z,r,0)$, μ_m is the mth zero of the zeroth-order Bessel function J_0, and the decay rates are defined by

$$\Gamma_{mn}=\frac{\Gamma_{\rm SD}}{S}+\left[\frac{n^2\pi^2}{l^2}+\frac{\mu_m^2}{a^2}\right]D\ . \tag{36}$$

This is an exact solution, independent of the initial polarization distribution developed in the cell, and also applies in the case of an optically thick vapor and for large polarizations. Equation (35) shows that diffusion gives rise to a polarization distribution in the cell which is comprised of various modes. Since the polarization in optically thick cells varies strongly throughout the cell, higher-order diffusion modes are important. These diffusion modes relax at different rates, so that the transients are nonlinear. In order to extract a single rate constant which relates to the spin destruction rate, we must determine the effect of these various modes on the polarization decay.

To solve this problem for large optical thickness and large polarizations, a computer simulation was performed to determine whether the spin destruction rate could accurately be determined from the time transients. The program was designed to determine an initial polarization distribution given the incident light intensity, Rb number density, and spin destruction rate using the methods discussed in Sec. III. We then used standard integration techniques to determine the polarization at each point in the cell as the polarization decays.

A calculation of the time dependence of the average polarization shows that the decay is indeed nonexponential but can be described well by the first diffusion mode for times after 5 ms. A simple explanation of this result is possible by examination of the decay mode rates in Eq. (36). The cell geometry used for all the experiments and for the calculation here has a length of 2.5 cm and a radius of 0.6 cm. Thus the bulk of the polarization probed is affected more strongly by the radial walls than by the front and rear walls, i.e., most atoms are closer to the radial walls. So the majority of the polarization in the cell decays in modes characterized by μ_m^2, which rises rapidly with mode number. In addition, the nuclear-spin-slowing factor S depends on the polarization, and therefore also contributes to nonexponential decay. Numerical simulations show that waiting for the polarization to decay to below 30% is adequate for fitting to a single exponential.

In conclusion, the effects of nuclear-spin and wall relaxation both lead to nonexponential decay of the polarization. However, for sufficiently long times after the pumping light has been extinguished, when the low polarization limit is valid, the polarization time transients can be described accurately by a single exponential. The decay is thus given by

$$\frac{d\bar{P}_{\rm Rb}}{dt}=\frac{\Gamma_{\rm SD}}{10.8}+\left[\frac{\pi^2}{l^2}+\frac{\mu_1^2}{a^2}\right]D\ , \tag{37}$$

where $\mu_1=2.405$ is the first zero of J_0.

A. Relaxation in the dark

The technique used to measure the electron randomization rates was a variation of the method developed by Franzen [31]. This involves producing a large polarization in the vapor with a strong pump source, abruptly shutting off the pumping light and detecting the decaying polarization with a weak probe. The experimental setup is similar to that used for the polarization versus wavelength scans (shown in Fig. 3). The Ti:sapphire pump beam was turned on and off by an optical chopper spinning at 4 Hz with a duty cycle of 10%. The pump power was set at 1 W or greater, so the 20-ms time interval during which the beam was unblocked was more than enough time to fully polarize the vapor (i.e.,

$\gamma_{opt}/S \gg 1/20$ ms). The optical chopper triggered the data collection by sending a pulse to the computer each time the pump beam was unblocked. The polarization was monitored by lock-in detection of the PEM-modulated probe beam as described in Sec. III B. Data were taken during the entire "dark" cycle. The cycle was then repeated, typically 256 times, and the data were averaged. The transmission of the probe at dc was also monitored to provide a measure of the relative Rb number density.

The functional form to which the data were fit was

$$A + B \sinh(Ce^{-\Gamma t}) \tag{38}$$

where A accounts for an offset in the lock-in signal, B is related to the probe attenuation, C is related to the inverse probe absorption length and the initial Rb polarization, and Γ is the total spin-relaxation rate. The sinh dependence follows from the difference in transmission signal between σ_+ and σ_- light. A typical data set is shown in Fig. 12(a) for $T = 160$°C and Rb number density 1.3×10^{14} cm^{-3}. The nonexponential behavior for the first 20 ms of the decay is very clear. In Fig. 12(b), we plot the residuals of the data from a fit at times $t > 30$ ms.

The data analysis depends on the ability to determine at what time after the start of the decay the data were accurately described by a single exponential decay constant. To do this, we fit the data to a single exponential with variable starting time after the pump laser was switched off. As the starting time was increased, the χ^2 per degree of freedom decreased. The valid starting time was determined when χ^2/N no longer changed.

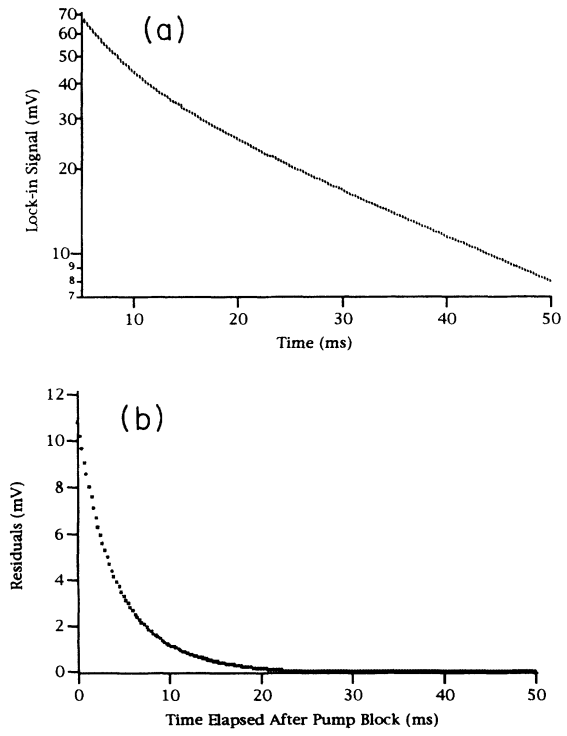

FIG. 12. (a) Decay of Rb polarization showing nonexponential behavior. (b) Residuals from a fit of the data after 30 ms to a single exponential decay constant.

1. Rb density measurements

The Rb density was determined by a combination of absorption and Faraday rotation [28] techniques. The measurements using the sealed cells were performed using Faraday rotation, and were constrained to temperatures below 190°C. For the valved cell measurements we used the absorption technique, tuning very far off the resonance (up to 15 linewidths). Measurements were made at temperatures up to 220°C. The pressure broadening of the cell for these measurements was 15 GHz. We then used the Faraday rotation technique at 150 and 160°C with a buffer-gas pressure of 100-torr N_2 (2-GHz linewidth) to cross calibrate the density measurements. The data are consistent with the vapor pressure curves of Killian [27] for the sealed cell and at the lower temperatures for the valved cells. The Rb density depends crucially on the distribution of the condensed Rb on the cell wall and the positioning of the temperature monitors. Therefore, the Rb density at higher temperatures is likely to vary from cell to cell, and direct measurement of the number density for experiments with high cell temperatures is crucial.

The uncertainty in density measurements was dominated by a statistical error in the fitting of Faraday rotation signals and the uncertainty in the wavelength calibration. Additionally, the absolute rotation calibration and the magnetic-field measurement each add approximately 1% to the error. As an example, the density at 150°C in the valved cell was

$$[\mathrm{Rb}] = (0.794 \pm 0.038) \times 10^{14} \text{ cm}^{-3}$$

representing a 4.8% error in the density determination.

2. Rb-Rb spin destruction collisions: results

Measurements of the Rb-Rb collision-induced relaxation rate constant were performed using the polarization transient measurement technique described above. For these data the Rb number density was varied between 0.5 and $12 \times 10^{14}/\text{cm}^3$. As discussed above, the density measurements were accomplished by keeping the diode laser tuning parameters fixed and using the dc transmission as a measure of the relative Rb density. Although the long term drift of the diode laser was determined to be very small, precautions were taken to eliminate systematic errors introduced by drifting of the diode laser intensity. To this end, the measurements were performed by taking data in two steps: First the relaxation rates were measured in steps of increasing density, and a second set of measurements was then done while decreasing the density. As a second precaution, the diode laser tuning was not changed during the entire data set. Because of this requirement the measurements were constrained to the above-quoted density range, within which a good absorption signal could be obtained at a single-probe laser tuning. Calibration of the transmission measurements was

done via Faraday rotation prior to each data run at two temperature settings, usually 150 and 160°C.

The error for these measurements was due mostly to error in the Faraday rotation calibration and to statistical error in fitting the time transients. The errors in the fitting were actually found to be much smaller than the fluctuations of the measured relaxation rate from run to run. This is most probably due to nonlinear effects which might affect each run differently depending on how well it was fit to a single exponential. Therefore, each transient was measured three times, and the final result was an average of these measurements with the total error in the rate determination given by the fluctuations in the rate. In addition, a small contribution is due to errors in the relative density measurements.

The results of two data sets illustrating spin destruction due to Rb-Rb collisions are plotted in Fig. 13. The solid lines are fits to each data set from which the rate constant ($k_{SD}=\langle\sigma_{SD}v\rangle$) is given by the slope of the best fit. The results for the rate constant for this process are $k_{Rb\text{-}Rb}=(7.98\pm0.41)\times10^{-13}$ cm^3/s and $(8.35\pm0.55)\times10^{-13}$ cm^3/s, for the 400- and 800-torr data sets, respectively. These numbers assume the low polarization limit of 10.8 for the slowing factor. As mentioned previously, all aspects of the experiment were repeated for the two measurements, including the Faraday rotation calibration, so the two numbers quoted are not correlated and may be combined to obtain the final result:

$$k_{Rb\text{-}Rb}=(8.11\pm0.33)\times10^{-13}\text{cm}^3/\text{s}\ .$$

This is in good agreement with a recent measurement of Knize [32]:

$$k_{Rb\text{-}Rb}=(7.8\pm0.8)\times10^{-13}\text{cm}^3/\text{s}\ .$$

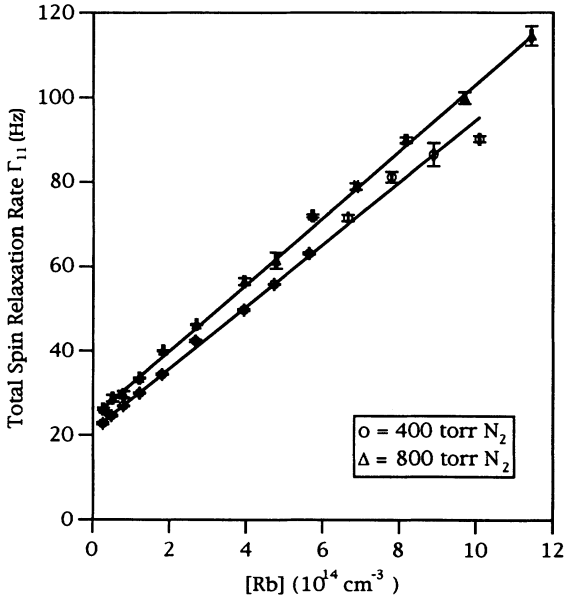

FIG. 13. Final results of the Rb-Rb spin destruction rate measurements at densities of $0.5-12\times10^{14}$ cm^{-3} for N_2 buffer-gas pressures of 400 and 800 torr.

B. Rb-buffer-gas spin destruction collisions

Although the cross sections for spin destruction due to Rb-N_2, Rb-^{3}He, and Rb-^{4}He collisions have been measured previously [33–36], there was sufficient question as to the validity of these measurements to warrant repeating them. For instance, a full understanding of the effects of diffusion modes on the relaxation of the polarization was not developed until many years later. In addition, a more recent determination of the Rb-N_2 diffusion constant is in disagreement with that measured by McNeal [34].

Assuming a single diffusion mode can be extracted from the data, the spin destruction rate is given by

$$\Gamma_{11}(p)=\left[\frac{\pi^2}{l^2}+\frac{\mu_1^2}{a^2}\right]D_0\left[\frac{p_0}{p}\right]+N_0\frac{\langle\sigma_{SD}v\rangle}{S}\left[\frac{p}{p_0}\right], \tag{39}$$

where p_0 and D_0 are the atmospheric pressure and diffusion constant at standard pressure (760 torr), and N_0 is a conversion factor from number density to pressure. The low polarization limit is assumed by setting $S=10.8$. The relaxation rates were measured for [Rb] between 1 and 4×10^{14} cm^3 and extrapolating to zero density. The transients were measured three times at each density to estimate the error due to additional diffusion modes in the decay. The sources of error are the same as the Rb-Rb case, except there are added uncertainties due to the extrapolation and the ^{3}He buffer-gas pressure determination. Figures 14 and 15 show relaxation rates as a function of N_2 and ^{3}He pressure, respectively. The solid lines are fits to the functional form of Eq. (39).

The data show fluctuations larger than those that would be consistent with the assumed errors. One possible cause of the fluctuations is the presence of impurities in the cell, as first noted by Franz [35]. For an impurity partial pressure of 1×10^{-6} torr, and assuming a large, spin-exchange-like interaction ($\sigma\sim10^{-14}$ cm^2), the impurities could increase the relaxation rate by approximately 3–5 Hz. This is consistent with the fluctuations seen in Fig. 14, which were measured twice, and with the large variations seen in the ^{3}He data. The implications of

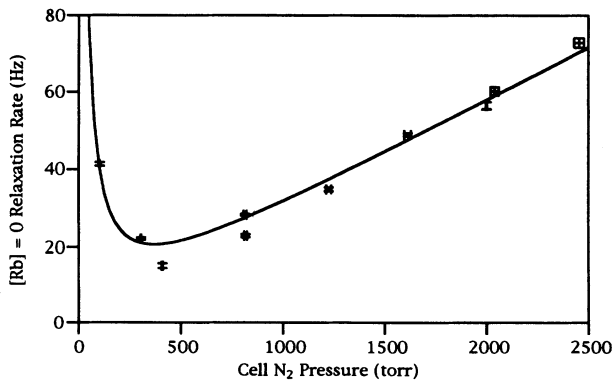

FIG. 14. Spin-relaxation rate as a function of the N_2 buffer-gas pressure measured by extrapolating polarization transient rates to zero Rb density as described in the text.

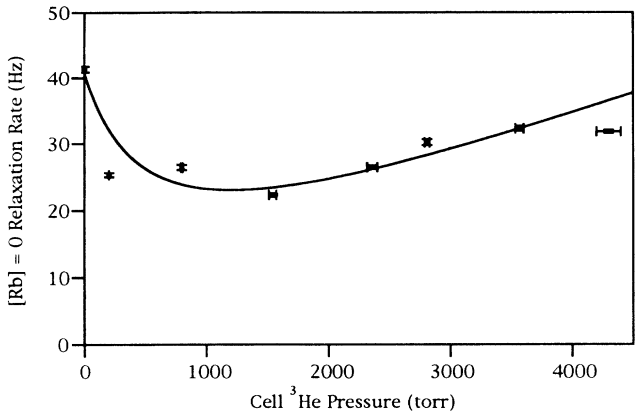

FIG. 15. Spin-relaxation rate as a function of the ^{3}He buffer-gas pressure. 100 torr of N_2 was included in each fill for radiation-trapping quenching.

such an effect on the relaxation cross section measurements will be discussed below.

The results for the spin destruction rate constants are

$$k_{N_2\text{-Rb}}=(9.38\pm0.22)\times10^{-18}\text{cm}^3/\text{s}\ ,$$

$$k_{^3\text{He-Rb}}\leq(2.29\pm0.23)\times10^{-18}\ \text{cm}^3/\text{s}\ .$$

In terms of buffer-gas pressure, these results may be interpreted to yield rates of 0.302 ± 0.007 and 0.074 ± 0.008 Hz/torr for N_2 and ^{3}He, respectively. The data also provide a measure of the Rb-buffer-gas mutual diffusion constants. They are

$$D_0(\text{Rb-N}_2)=0.28\pm0.02\ \text{cm}^2/\text{s}\ ,$$

$$D_0(\text{Rb-}^3\text{He})=1.5\pm0.4\ \text{cm}^2/\text{s}$$

at 150°C. These can be compared with earlier measurements of mutual diffusion constants. Zeng *et al.* [13] obtained $D_0(\text{Rb-N}_2)=0.20$ cm^2/s at 70°C. Assuming a $T^{3/2}$ temperature dependence, this becomes to 0.27 cm^2/s at 150°C, in excellent agreement with our measurement. $D_0(\text{Rb-}^3\text{He})$ has been measured most recently by Aymar, Bouchiat, and Brossel [36] to be 0.53 ± 0.08 cm^2/s at 27°C, which translates to 0.89 ± 0.13 cm^2/s at 150°C. Within experimental error, this is also in agreement with the result quoted above. This confirms the validity of assuming a single diffusion-mode relaxation for all of the spin destruction results presented above.

Comparison of the Rb-buffer-gas spin destruction rate constants with previous measurements, on the other hand, shows large discrepancies. The result obtained by McNeal [34] is 1.28 Hz/torr for Rb-N_2. Our measurement of a smaller rate constant for Rb-N_2 collisions, however, is not too surprising. The diffusion constant measured by McNeal is almost a factor of 2 too large, indicating that the experiment may have been flawed by not properly accounting for higher-order diffusion-mode relaxation. It is also possible that impurity partial pressures contributed to the spin destruction, increasing the rate constant measured by McNeal [34].

For Rb-^{4}He, Bernheim and Franz report 0.047 and 0.021 Hz/torr, respectively [33,35]. A subsequent measurement by Aymar, Bouchiat, and Brossel [36] for Rb-^{4}He is in agreement with the results of Franz, and also shows no difference in cross section between Rb-^{4}He and Rb-^{3}He (the spin-exchange contribution to the measured relaxation rate would negligibly change the Rb-^{3}He rate constant: using the result of Coulter [14], the contribution would be 0.004 Hz/torr). Our result for the Rb-^{3}He rate constant is larger than these two results. It is possible that a significant impurity partial pressure was present which flawed the measurement. However, the measurement was made as a function of ^{3}He pressure, so that the impurity gases would have to be found in the ^{3}He gas introduced into the cells. Using the result of Aymar, Bouchiat, and Brossel [36], this would indicate an impurity relaxation of 0.05 Hz per torr of ^{3}He. Again assuming a large, spin-exchange-type cross section due to the paramagnetic impurities in ^{3}He, this would only require an impurity partial pressure of one part in 10^{10} in the ^{3}He gas bottle. The ^{3}He used here had a purity of ≤ 10 ppm. It would therefore seem a difficult task to obtain the necessary purity of ^{3}He. In any event, the measurements here have demonstrated that a large spin-relaxation rate can be encountered in the presence of a large buffer-gas pressure; it has to be determined whether this relaxation is due to collisions with ^{3}He or with impurity gases introduced with the ^{3}He.

We note that Ref. [16] reports evidence of a term in Γ_{SD} proportional to $[^3\text{He}]^2$ in the measurement of transmitted circularly polarized optical-pumping light. However, that analysis constrains $k_{^3\text{He-Rb}}$ to the value derived from a measurement of spin-exchange relaxation of polarized ^{3}He which is smaller by a factor of 2 than previous measurements [14] and does not include the contribution due to spin rotation.

In conclusion, we have presented a method for accurately measuring spin destruction cross sections in dense alkali-metal vapors. The measurement of a large Rb-Rb spin destruction rate constant would indicate that the process involved is a magnetic dipole-dipole interaction which leads to a significant spin-flip probability during an atomic collision. This spin destruction mechanism clearly leads to a large decrease in the optical-pumping efficiency of vapors at high densities. Measurements of alkali-metal–buffer-gas rate constants have also been presented. For Rb-N_2, they produced a rate constant which is a factor of 3 smaller than previously measured, indicating that the presence of 100–200 torr of a N_2 quenching buffer gas will not seriously affect the optical pumping of the alkali-metal vapor. The rate constant measured for Rb-^{3}He is a factor of 2–3 larger than three previous measurements, and due to the possibility of spin-relaxation contributions from impurity gases should be considered an upper limit. Using the upper limits for Rb-buffer-gas collisions, we can write

$$\Gamma_{SD}=k_{\text{Rb-Rb}}[\text{Rb}]+k_{^3\text{He-Rb}}[^3\text{He}]+k_{N_2\text{-Rb}}[N_2]\ . \quad (40)$$

V. APPLICATION TO HIGH-DENSITY-POLARIZED ^{3}HE TARGETS

The analyses presented in this paper have demonstrated two important concepts in the polarization of a high-density alkali-metal vapor. The first is the existence of spin-destroying collisions in the vapor. For densities above approximately $5\times10^{14}/\text{cm}^3$, spin destruction due to alkali-alkali collisions presents a serious limitation to the polarization process and necessitates the input of high laser intensity to offset this effect. In addition, collisions with buffer-gas atoms begin to play an important role for high buffer-gas pressures. Rb-^{3}He collisions become important at ^{3}He pressures of approximately 5 atm and above. The second concept is that of wall-induced relaxation which, along with atomic diffusion, leads to the creation of a finite thickness boundary layer at the cell walls which strongly absorbs the incoming laser intensity. This has been shown to limit the polarization attainable in a dense vapor under certain conditions. With the benefit of this knowledge, we have developed a detailed model of the alkali-metal vapor polarization spatial profile which can be used to predict the polarization limitations for any given situation.

The last few years have seen the spin-exchange–optical-pumping technique for producing polarized ^{3}He targets used for a number of exciting nuclear and high-energy physics applications [5–9]. To conclude this paper, we present the results of specific calculations which relate to the polarized ^{3}He target applications. As an example, we consider the polarized ^{3}He targets used at Standford Linear Accelerator Center (SLAC) and Bates linear accelerator for recent measurements of the spin-dependent structure function of the neutron by deep inelastic scattering of 20–25-GeV polarized electrons from the polarized ^{3}He [9] and the neutron's elastic form factors [8]. The polarized ^{3}He target was chosen for these measurements since the nucleus of ^{3}He consists of two protons and one neutron, and the dominant part of the nuclear wave function is a symmetric s state with the two proton spins paired [37]. Thus a polarized ^{3}He nucleus consists of a highly polarized neutron with dilution by the presence of the protons.

In both cases, the targets consisted of two chambers in order to separate the optical-pumping region from the region through which the electron beam passes [7]. This reduces the spin exchange rate by a factor of 2. For the SLAC target, the optical-pumping region is a cylinder with $l=5.1$ cm and $d=5$ cm, pumped along its axis. The experimental parameters are laser power of approximately 10–15 W, and buffer gases of 9 atm ^{3}He and 100-torr N_2 (both at 300 K). In this case, ^{3}He-Rb collisions contribute significantly to the total spin destruction rate and place a significant limitation on the maximum Rb density which can be polarized. We can produce a rough estimate of the polarization limitations imposed by spin destruction. The relationship of laser power, intensity, and [Rb] is given by

$$\frac{P_{\text{laser}}}{h\nu}e^{-nl_D/\lambda_0}=\Gamma_{\text{SD}}[\text{Rb}]V\ , \tag{41}$$

where P_{laser} is the total laser power and V is the total optical-pumping volume. For 10 W and $I_0=500$ mW/cm^2 and $n=1$ (the high buffer-gas pressure limit), we expect a Rb polarization of 1 for Rb densities below approximately 1.5×10^{14} cm^{-3}. Figure 16 shows the predicted ^{3}He polarization as a function of Rb density for the SLAC target cell with 10 W of incident laser power. We have used the observed 1/(40 hr) ^{3}He wall relaxation rate. For the SLAC target, the ratio $l_D/\lambda_0=0.025$, and from Figs. 9 or 10 it is apparent that the dip phenomenon is negligible due to the high buffer-gas pressures and correspondingly small resonant absorption cross section. Therefore we expect maximum polarization to be attained with on resonance radiation for all values of [Rb] considered. In Fig. 16 we also show a single data point corresponding to the actual performance of the SLAC target. The Rb number density was estimated on the basis of the ^{3}He spin-exchange time constants. In the final analysis, large ^{3}He polarizations (approximately 50%) should have been obtained for the SLAC target, if care had been taken in considering the optimum Rb number density and the laser beam geometry.

For the Bates target, the pumping cell was also a cylinder with $l=7$ cm and $d=2.1$ cm. The laser light was incident at various angles with respect to the cylinder axis; however, the best performance was achieved with the laser light directed along the cylinder axis. The available laser power was about 3 W, and the target contained buffer gases of 3.5 atm ^{3}He and 100-torr N_2 (both at 300 K). The ratio $l_D/\lambda_0=0.13$, and in this case the lower buffer-gas densities, result in larger $D1$ absorption cross sections for Rb. From Figs. 9 or 10, it is apparent that the boundary layer and dip phenomena play an important role. It has been customary to tune the laser slightly off-resonance, so that a smaller fraction of the incident

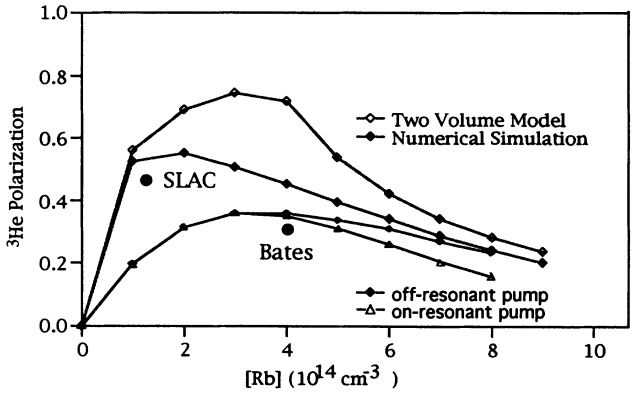

FIG. 16. Plot of calculated maximum ^{3}He polarization as a function of Rb number density for the SLAC and Bates polarized ^{3}He targets. For the SLAC target, we present results assuming the naive two-volume model and a realistic numerical simulation. For the Bates target, we show the effects of the common practice of tuning the laser off-resonance. Also shown for both targets are approximations of the actual performances for the two experiments. The incident dimensions, pressures, and laser powers used in the calculations are presented in Sec. V of the text. The calculations assume the Rb spin destruction rate given by Eq. (40).

light is wasted in that layer. In Fig. 16, we show the results of calculations for the Bates target for incident power of 3 W, and the laser tuned on-resonance and off-resonance by an amount that allows the center of the laser beam to penetrate to the end of the pumping cell. Also shown in Fig. 16 is the approximate actual performance of the Bates target [7], which is in good agreement with the simulations.

Also shown in figure 16 is the expectation of the simple two-volume model for the SLAC target. The results of the two-volume model place only an upper limit on the maximum vapor polarization that depends exclusively on the total available laser *power*. In other words, for a given Rb density the largest volume which can be polarized is limited only by the laser power. The results presented here, however, illustrate that, because of diffusion effects, the laser intensity is also a quantity of importance. Therefore, additional limitations are placed on the vapor polarization by the cell and optical-pumping laser *geometry*. Of course, a second important factor is the buffer-gas pressure, which is effective in mitigating diffusion effects by decreasing the cross section for absorption of incident light. These two statements provide the essence of the lessons to be extracted from this paper.

VI. SUMMARY

We have presented studies of high-density Rb optical pumping under conditions encountered in polarized ^{3}He targets. A theoretical model of the polarization has been developed, along with numerical methods for determining the spatial polarization distribution in the dense alkali-metal vapor. We show how the boundary layer is formed, and derive the spatial distribution of polarization within this layer. This effect can lead to a significant wavelength-dependent decrease in the optical-pumping efficiency. The crucial result is that even for buffer gas pressures on the order of 11 atm, optical pumping at high vapor densities is impeded by wall relaxation. The presence of very large buffer-gas pressures helps to mitigate these effects, not by impeding diffusion of the atoms to the cell wall, but by diminishing the resonant absorption cross section, thereby decreasing the absorption of light within the diffusion boundary layer. The important practical result is that not only total laser power but also local laser intensity need to be considered when developing a spin-exchange–optical-pumping gas target. The intensity dependence of the boundary layer thickness suggests that increased laser intensity is necessary to compensate. However high-intensity effects are also possible. For extremely high intensity (on the order of 100 W/cm^3) we have qualitatively observed effects that may be attributed to localized radiation trapping due to dissociation of the N_2.

In order to perform measurements in the dense vapors, experimental techniques have been presented and used to measure wavelength dependence of Rb polarization and spin-destroying collisions with other Rb atoms and buffer-gas molecules. We have demonstrated the success of the modeling of the wavelength dependence and characterization of resonant polarization dips. Our measurements of bulk relaxation show that for ^{3}He densities on the order of several atmospheres, Γ_{SD} is significantly increased. High-intensity and residual radiation trapping effects are also possible and remain to be investigated.

ACKNOWLEDGMENT

This work was supported in part by the National Science Foundation.

[1] T. E. Chupp, E. R. Oteiza, J. M. Richardson, and T. R. White, Phys. Rev. A **38**, 3998 (1988).
[2] M. T. Myint, Ph.D. thesis, Harvard University, 1969 (unpublished); H. G. Robinson and M. T. Myint, Appl. Phys. Lett. **5**, 116 (1964).
[3] M. G. Richards, B. P. Cowan, M. F. Secca, and K. Machin, J. Phys. B **21**, 665 (1988).
[4] B. Wu, R. Walsworth, R. J. Hoare, and T. E. Chupp (private communication).
[5] B. Larson *et al.*, Phys. Rev. Lett. **67**, 3356 (1991).
[6] N. Newberry *et al.*, Phys. Rev. Lett. **67**, 3219 (1991).
[7] T. E. Chupp, R. A. Loveman, A. K. Thompson, A. M. Bernstein, and D. R. Tieger, Phys. Rev. C **45**, 915 (1992).
[8] A. K. Thompson *et al.*, Phys. Rev. Lett. **68**, 2901 (1992).
[9] P. L. Anthony *et al.*, Phys. Rev. Lett. **71**, 959 (1993).
[10] T. E. Chupp, M. E. Wagshul, K. P. Coulter, A. B. McDonald, and W. Happer, Phys. Rev. C **36**, 2244 (1987).
[11] M. A. Bouchiat, T. R. Carver, and C. M. Varnum, Phys. Rev. Lett. **5**, 373 (1960).
[12] W. Happer, Hyp. Int. **38**, 435 (1987).
[13] X. Zeng, Z. Wu, T. Call, E. Miron, D. Schreiber, and W. Happer, Phys. Rev. A **31**, 260 (1985).
[14] K. P. Coulter, Ph.D. thesis, Princeton University, 1989 (unpublished).
[15] A. Abragham, *Principles of Nuclear Magnetism* (Oxford University Press, Oxford, 1961), p. 352; N. Newberry *et al.*, Phys. Rev. A **48**, 4411 (1993).
[16] B. Larson *et al.*, Phys. Rev. A **44**, 3108 (1991).
[17] M. E. Wagshul and T. E. Chupp, Phys. Rev. A **24**, 827 (1989).
[18] A. Gallagher, Phys. Rev. A **157**, 68 (1967); **163**, 206 (1967).
[19] S.-Y. Ch'en and M. Takeo, Rev. Mod. Phys. **29**, 20 (1957).
[20] H. Margenau and W. H. Watson, Rev. Mod. Phys. **8**, 22 (1936).
[21] H. M. Gibbs and R. J. Hull, Phys. Rev. **153**, 132 (1967).
[22] L. W. Anderson, F. M. Pipkin, and J. C. Baird, Phys. Rev. **120**, 1279 (1960).
[23] M. B. Gornyi and B. G. Matisov, Opt. Spektrosk. **56**, 620 (1984) [Opt. Spectrosc. (USSR) **56**, 380 (1984)]
[24] F. Masnou-Seeuws and M. Bouchiat, J. Phys. (Paris) **28**, 406 (1967).
[25] D. R. Swenson and L. W. Anderson, Nucl. Instrum. Methods Phys. Res. B **29**, 627 (1988).
[26] M. E. Wagshul, Ph.D. dissertation, Harvard University, 1991 (unpublished).
[27] T. J. Killian, Phys. Rev. **27**, 578 (1926).
[28] Z. Wu, M. Kitano, W. Happer, M. Hou, and J. Daniels, Appl. Opt. **25**, 4483 (1986).

[29] M. A. Bouchiat and J. Brossel, Phys. Rev. **147**, 41 (1966).
[30] P. Minguzzi, F. Strumia, and P. Violino, Nuovo Cimento **46B**, 145 (1966).
[31] W. Franzen, Phys. Rev. **115**, 850 (1959).
[32] R. J. Knize, Phys. Rev. A **40**, 6219 (1989).
[33] R. A. Bernheim, J. Chem. Phys. **36**, 135 (1962).
[34] R. J. McNeal, J. Chem. Phys. **37**, 2726 (1962).
[35] F. A. Franz, Phys. Rev. **139**, A603 (1965).
[36] M. Aymar, M. A. Bouchiat, and J. Brossel, J. Phys. (Paris) **30**, 619 (1969).
[37] J. L. Friar, B. F. Gibson, G. L. Payne, A. M. Bernstein, and T. E. Chupp, Phys. Rev. C **42**, 2310 (1990).